Palestinian Medical and Pharmaceutical Journal

Mechanistic In Silico Analysis of *Rolandra Fruticosa* Sesquiterpenes Targeting Anti-Apoptotic Pathways in Colorectal Cancer

Hung Duc Nguyen[1]*

(Type: Full Article). Received: 9th Jan. 2026. Accepted: 1st Mar. 2026, Published: ××××, DOI: ××××

Accepted Manuscript, In Press

Abstract: Background: Colorectal cancer continues to impose a substantial global health burden, with GLOBOCAN 2022 estimating approximately 1.93 million new cases and 0.90 million deaths. Resistance to therapy remains a major limitation, highlighting the need for strategies that restore apoptosis and target anti-apoptotic Bcl-2 family proteins. Myeloid cell leukemia 1 (Mcl-1), a key pro-survival regulator implicated in chemoresistance, including in colorectal cancer, therefore represents a promising molecular target. **Methods:** This study evaluated a sesquiterpene-derived candidate (CPD2) from Rolandra fruticosa against Mcl-1 (PDB: 6QFQ) using an integrated in silico workflow. The analyses included molecular docking, molecular dynamics (MD) simulation, MM/GBSA end-point free-energy estimation, ADMET prediction using pkCSM, and density functional theory (DFT)-based electronic descriptors. Fruquintinib, an approved anticancer agent, was used as the reference compound. **Results:** Docking analysis positioned CPD2 within the canonical BH3-binding groove of Mcl-1 and suggested favorable interactions with hotspot residues, including Arg263. Over 100 ns of MD simulation, the CPD2–Mcl-1 complex exhibited a comparatively restrained conformational ensemble, whereas the fruquintinib complex showed greater deviation during the later stage of the trajectory. MM/GBSA analysis supported favorable binding for both ligands, although fruquintinib displayed a more favorable mean binding free energy under the applied protocol. ADMET prediction indicated that CPD2 had fewer predicted CYP inhibition liabilities and safety-alert signals than fruquintinib, despite showing distinct absorption–clearance trade-offs. DFT descriptors further suggested greater electronic responsiveness for CPD2. **Limitations:** A key limitation of this study is its reliance on model-dependent assumptions, including the use of a single receptor conformation and limited dynamical sampling. These findings therefore require confirmation through biochemical, cellular, pharmacokinetic, and toxicity studies. **Conclusion:** Overall, the computational evidence identifies CPD2 as an optimization-relevant scaffold targeting Mcl-1 and supports its prioritization for further experimental validation.

Keywords: anti-apoptosis, colorectal cancer, in silico, Mcl-1, *Rolandra fruticosa*, sesquiterpenes.

Introduction

Colorectal cancer presents a significant worldwide health challenge, with the GLOBOCAN 2022 data from the International Agency for Research on Cancer reporting an estimated 1,926,425 new cases and 904,019 deaths globally in 2022. This accounts for 9.6% of all new cancer diagnoses and 9.3% of total cancer deaths, making mortality from this malignancy the second leading cause of cancer death in the world [1]. In Viet Nam, colorectal cancer ranked fourth for incidence across both sexes, with 16,835 new cases in 2022, while mortality ranked fifth, with 8,454 deaths. Therapeutic development increasingly emphasizes biomarker-informed approaches, including molecularly targeted agents for metastatic colorectal cancer, alongside strategies intended to mitigate or delay treatment failure driven by acquired resistance [2,3]. A central biological rationale for several anticancer strategies involves restoration of regulated cell death. The Bcl-2 protein family is a pivotal regulator of mitochondrial outer membrane permeabilization and apoptotic commitment, while also exerting non-canonical control over intracellular signaling networks [4]. In particular, Bcl-2 family members participate in mitochondria-endoplasmic reticulum calcium regulation, with downstream effects on mitochondrial calcium homeostasis and cellular bioenergetics, thereby influencing survival-death decisions beyond apoptosis alone [5].

Mcl-1 (myeloid cell leukemia 1) constitutes a principal pro-survival member of the anti-apoptotic Bcl-2 protein network that preserves mitochondrial integrity and constrains commitment to intrinsic apoptosis. Mechanistically, Mcl-1 sequesters BH3-containing pro-apoptotic partners and functionally neutralizes pore-forming effectors such as BAX/BAK, thereby preventing mitochondrial outer membrane permeabilization and subsequent cytochrome c release. Aberrant Mcl-1 upregulation has been documented across multiple malignancies. It has been linked to reduced sensitivity to cytotoxic and targeted agents, consistent with a role in therapy resistance and adverse clinical outcomes. Consequently, pharmacologic inhibition of Mcl-1, including BH3-mimetic and related strategies, has emerged as a rational antineoplastic approach aimed at restoring apoptotic susceptibility in Mcl-1-dependent tumor contexts [6,7]. In colorectal cancer models, DNA-damaging chemotherapy has been shown to promote nuclear translocation of MCL-1, contributing to chemoresistance in p53-deficient contexts and exposing a Bcl-xL co-dependency that can be therapeutically exploited; combination regimens incorporating Bcl-xL inhibition have therefore been explored as sensitization strategies [8-10].

1 Faculty of Biology, Thai Nguyen University of Education, Thai Nguyen, 24124, Viet Nam.
* Corresponding author: hungnd@tnue.edu.vn
Orcid iD: https://orcid.org/0000-0002-5764-1242

Natural products continue to be a major foundation for anticancer discovery and development. More than 60% of anticancer drugs in clinical use have been reported to originate from, or be inspired by, natural products derived from plants, marine organisms, and microorganisms [11]. The structural diversity and pleiotropic bioactivity of natural-product scaffolds support continued investigation as sources of leads capable of modulating multiple oncogenic pathways, including apoptosis-related networks relevant to Bcl-2 family regulation [12]. Given the favorable therapeutic profile of natural compounds in oncology, continued investigation of additional sources and mechanistic pathways remains essential for expanding treatment modalities.

Sesquiterpenes, a large class of natural plant-derived compounds, are being extensively investigated for their significant anticancer properties and potential use in developing new chemotherapeutic agents [13,14]. Previous studies have demonstrated that sesquiterpenes isolated from Rolandra fruticosa possess significant cytotoxic properties against colorectal cancer cell lines [15]. Notably, these compounds have shown substantial efficacy against HT-29 colon cancer cells, suggesting their potential as promising candidates for the development of novel anticancer therapies. The cytotoxicity of sesquiterpene lactones is often associated with electrophilic structural features that can perturb essential cellular regulatory pathways, thereby promoting tumor cell death through apoptosis-linked mechanisms. Nevertheless, the target-level molecular determinants of activity for R. fruticosa sesquiterpene constituents remain insufficiently characterized, particularly in studies employing structure-based computational analyses. Accordingly, the present study evaluates selected sesquiterpene candidates from R. fruticosa using complementary in silico approaches (molecular docking, molecular dynamics simulation, and ADMET prediction) to infer binding propensities toward colorectal cancer-relevant macromolecular targets and to estimate behavior in a biological milieu. The resulting hypotheses provide a rational basis for subsequent experimental verification through rigorous in vitro and in vivo assessment.

Materials and Methods

Structural preparation of selected ligands

These selected ligands, including 13-Acetoxyrolandrolide (CPD1) and 8-Desacyl-13-acetoxyrolandrolide-8-*O*-tiglate (CPD2), have molecular formulas of $C_{23}H_{28}O_9$ and $C_{24}H_{30}O_9$, respectively, with molecular weights of 448.1733 and 462.1890 *m/z*. The Fruquintinib, possessing a molecular formula of $C_{21}H_{19}N_3O_5$ and a molecular weight of 393.1325 m/z, was chosen as the positive control (Figure 1).

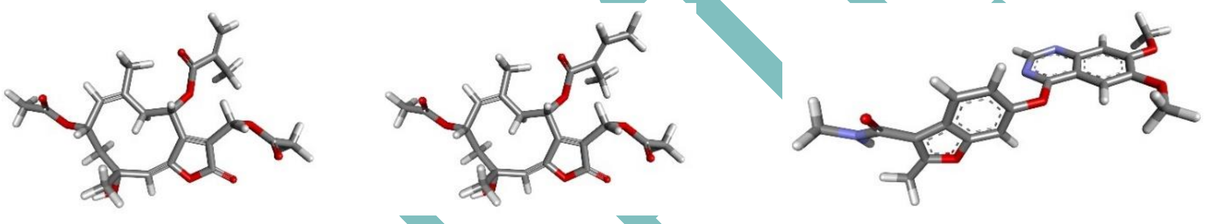

A B C

Figure (1): 3D Structures of selected ligands. (A) CPD1, (B) CPD2, and (C) Fruquintinib.

Molecular docking

Three-dimensional ligand geometries were generated and saved in PDB format using BIOVIA Discovery Studio Visualizer, followed by the addition of polar hydrogen atoms, assignment of Gasteiger partial charges, and designation of rotatable bonds as flexible. The X-ray crystal structure of the anti-apoptotic protein Mcl-1 (PDB ID: 6QFQ) was retrieved from the RCSB Protein Data Bank [16]. Docking simulations were performed using AutoDock Tools with a cubic grid box comprising 60 points in each of the x, y, and z dimensions, with a spacing of 0.375 Å, centered at x = 3.934 Å, y = −18.343 Å, and z = 18.680 Å, to cover the binding site region. Pose generation and scoring employed the Lamarckian genetic algorithm to support conformational exploration, energy-based ranking, and refinement of plausible interaction patterns. The highest-ranked protein-ligand complex was subsequently examined in Discovery Studio Client 2024, and the resulting interaction map was interpreted in comparison with the docking pose of Fruquintinib within the same Mcl-1 structure to delineate convergent and divergent binding features.

Molecular dynamics simulation

Molecular dynamics simulations were conducted to evaluate the time-dependent stability of the docked Mcl-1-ligand complex obtained from the Mcl-1 crystal structure (PDB ID: 6QFQ) over a 100 ns trajectory using GROMACS 2024.4 with the CHARMM36 force field [17]. Protein preparation involved the reconstruction of missing atoms and residues in the Swiss-PdbViewer [18], whereas CHARMM-compatible ligand topology and parameters were generated via [19]. The complex was placed in a triclinic periodic box and solvated with SPC water, followed by the addition of NaCl to 0.15 M to achieve electroneutrality and physiological ionic strength. Energy minimization was performed using the steepest-descent algorithm for 50,000 steps to alleviate steric clashes and unfavorable contacts. Equilibration was implemented as two consecutive 200 ps phases under the NVT and NPT ensembles at 300 K and 1 bar, respectively. Production simulations were conducted as three independent replicates, each extending to 100 ns with a 2 fs integration step, and trajectory frames were recorded at 10 ps intervals for subsequent analysis. Trajectory processing and visualization in Grace yielded canonical measures of conformational behavior, including root mean square deviation (RMSD), root mean square fluctuation (RMSF), radius of gyration (Rg), solvent-accessible surface area (SASA), and number of hydrogen bonds (Hbonds). Structural concordance among representative conformers was additionally assessed in UCSF Chimera (v1.13.3) by coordinate superposition to compare characteristic states across the simulated trajectories [20].

Molecular mechanics generalised Born surface area (MM/GBSA) analysis

Binding free-energy estimates for the CPD2-6QFQ and Fruquintinib-6QFQ complexes were calculated using the gmx_MMGBSA workflow under the CHARMM36 parameterization. The polar solvation contribution was computed with a generalized Born implicit-solvent model, while the non-polar term was approximated as a solvent-accessible surface area-dependent component. Energetic components were extracted from the molecular dynamics trajectories using 125 evenly distributed snapshots sampled at 80 ps intervals within an 80 ns evaluation window (20-100 ns). Mean values across this snapshot ensemble facilitated a quantitative comparison of ligand-protein interaction energetics and supported inference regarding relative binding propensity and the persistence of each complex over the analyzed segment of the simulations [21].

Assay protocol for ADMET prediction

Early-stage assessment of absorption, distribution, metabolism, excretion, and toxicity (ADMET) properties is essential for identifying potential pharmacokinetic constraints and safety concerns, thereby guiding compound prioritization and mitigating late-stage failure [22]. In this study, the pkCSM web server was employed to predict the ADMET profiles of CPD2 and Fruquintinib. The pkCSM framework utilizes graph-based molecular signatures to estimate descriptors encompassing absorption, distribution, metabolism, excretion, and toxicity, thereby enabling a systematic comparison of developability-relevant attributes between the evaluated compounds.

Quantum chemistry computation using the Density Functional Theory (DFT) method

Geometry optimization of CPD2 and Fruquintinib was carried out using the ORCA quantum-chemistry package (v6.1.0). Initial molecular structures were generated in Avogadro, and molecular-orbital inspection together with complementary electronic analyses was performed in IboView (v20211019). Density functional theory computations applied the B3LYP exchange-correlation functional with the 6-31G(d,p) basis set to obtain optimized minima and their corresponding electronic wavefunctions. Using the converged geometries, frontier-orbital energies for HOMO and LUMO were extracted, and the associated energy gap (ΔE) was determined. Conceptual DFT descriptors, including chemical potential (μ), electronegativity (χ), global hardness (η), softness (σ), and electrophilicity index (ω), were subsequently derived under a Koopmans-type approximation to facilitate interpretation of electronic structure features and comparative reactivity tendencies of the investigated compounds [23-25].

Results and Discussion

Molecular docking analysis

Molecular docking provides a structure-based rationale for compound activity by estimating the preferred orientation of a ligand within a receptor pocket and by resolving the noncovalent contacts that stabilize the complex. Contemporary docking practice commonly interprets predicted poses through energetic ranking and recurrence of pocket-lining residues, while recognizing that docking scores represent model-dependent approximations that require complementary validation in dynamics or free-energy calculations [26]. Docking of CPD1, CPD2, and the reference Fruquintinib against the anti-apoptotic protein Mcl-1 (6QFQ) indicated that all ligands occupy a closely overlapping region of the BH3-binding groove, a canonical druggable cavity characterized by clustered hydrophobic pockets and electrostatic hot spots.

Before docking the ligands into 6QFQ, the protocol was verified by re-docking the co-crystallized ligand (Figure 2). The re-docked pose reproduced the experimental orientation with good overlap, yielding an RMSD of 1.2256 Å, which supports the validity of the docking setup. In general, RMSD values below 2 Å are widely used as a criterion for an acceptable and reliable docking procedure [27]. The resulting poses were then ordered by binding score, with more favorable conformations corresponding to lower (more negative) predicted binding energies (kcal/mol).

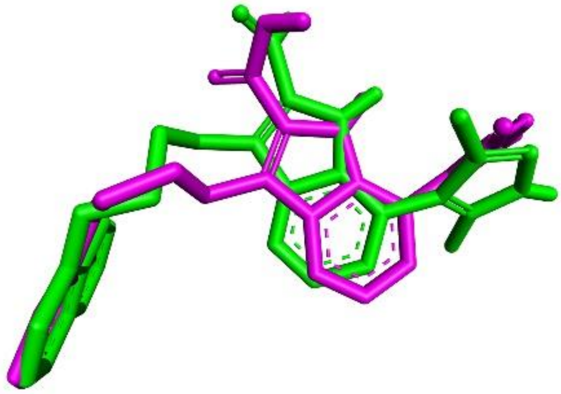

Figure (2): The superimposition of the docked and native ligands within 6QFQ protein for validation of the molecular docking protocol (violet = native, green = docked).

Among the tested molecules, CPD2 produced the most favorable docking energy (−8.80 kcal/mol), followed by CPD1 (−8.53 kcal/mol) and Fruquintinib (−8.33 kcal/mol), supporting a ranking of predicted retention within the groove as CPD2 > CPD1 > Fruquintinib under the applied scoring function (Table 1). The interacting residue sets converged on a conserved core that included Phe228, Met231, Val249, Met250, Val253, Arg263, and Phe270, consistent with recognition of the Mcl-1 BH3 groove through hydrophobic enclosure reinforced by a key polar/charged anchor region centered on Arg263 (Figure 3A) [28]. Interaction-pattern inspection revealed ligand-specific anchoring strategies that plausibly underlie the energetic ordering. CPD2 formed a hydrogen-bond contact with Arg263 and exhibited extensive hydrophobic engagement involving His224, Ala227, Phe228, Met231, Met250, Val253, Arg263, Leu267, and Phe270, together with van der Waals complementarity across Leu235, Leu246, Val249, Phe254, Gly262, and Thr266 (Figure 3B). Such a contact distribution suggests stabilization dominated by shape and dispersion complementarity within the hydrophobic pockets, supported by a single directional polar constraint at Arg263, a residue frequently described as a binding hot spot within the groove [29].

Table (1): The interactions between the docked ligands and the protein 6QFQ

Docked ligands	Binding energy (kcal/mol)	Hydrogen bond interaction	Van der Waals interaction	Hydrophobic interaction
CPD1	-8.53	His224, Phe254, Arg263, Leu267	Ala227, Leu235, Leu246, Val249, Thr266, Gly271, Val297	Phe228, Met231, Met250, Val253, Leu267, Phe270, Ile294
CPD2	-8.80	Arg263	Leu235, Leu246, Val249, Phe254, Gly262, Thr266	His224, Ala227, Phe228, Met231, Met250, Val253, Arg263, Leu267, Phe270
Fruquintinib	-8.33	-	Phe254, Arg263, Gly271, Leu290	Phe228, Met231, Leu235, Leu246, Val249, Met250, Val253, Thr266, Phe270, Val274, Ile294

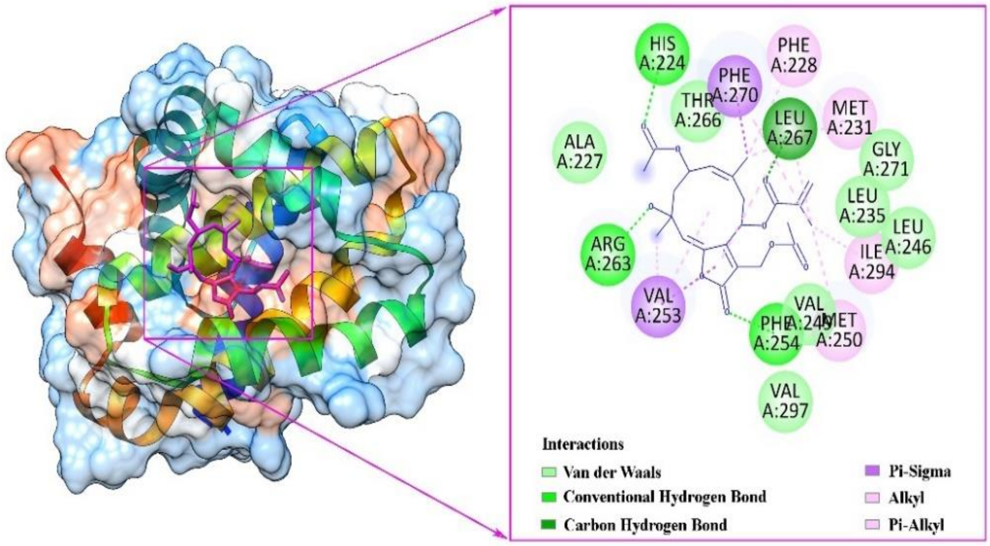

A

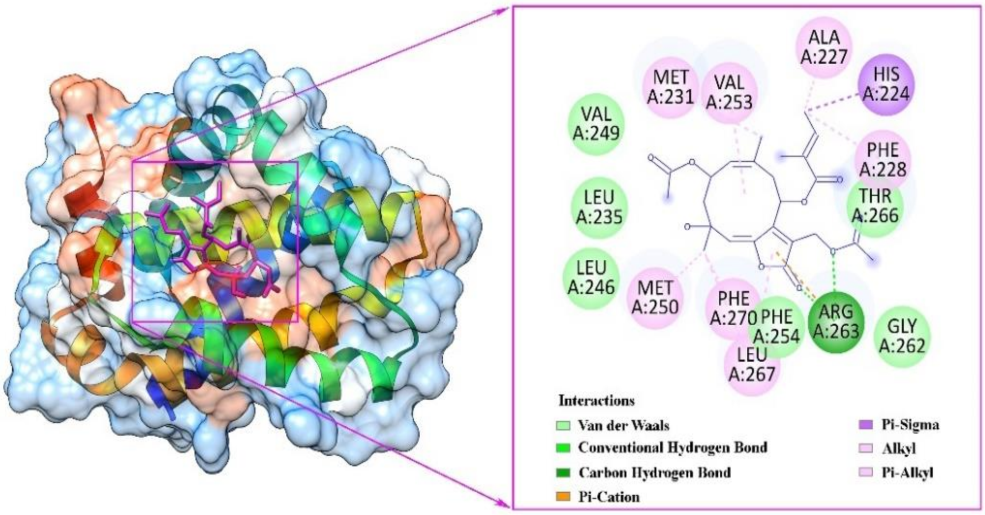

B

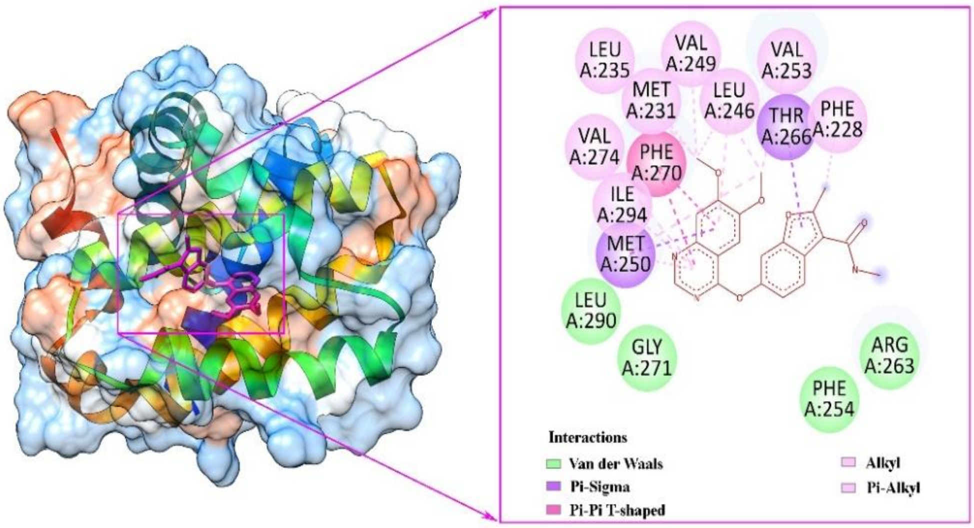

C

Figure (3): Molecular docking model and 2D interaction diagram of CPD1 (A), CPD2 (B), and Fruquintinib (C) with 6QFQ protein.

CPD1, despite a less favorable docking energy than CPD2, presented a denser polar-contact pattern (His224, Phe254, Arg263, and Leu267 annotated as hydrogen-bond partners) alongside hydrophobic packing with Phe228, Met231, Met250, Val253, Leu267, Phe270, and Ile294, and additional van der Waals contacts (Ala227, Leu235, Leu246, Val249, Thr266, Gly271, and Val297). This combination of polar anchoring and broad pocket complementarity remains consistent with productive groove occupancy. At the same time, the modestly weaker docking energy relative to CPD2 may reflect differences in how the scaffold optimizes hydrophobic pocket filling or steric fit. Fruquintinib displayed no hydrogen-bond assignment in the docking pose and relied primarily on hydrophobic and aromatic contacts (Phe228, Met231, Leu235, Leu246, Val249, Met250, Val253, Thr266, Phe270, Val274, and Ile294), with van der Waals contributions from Phe254, Arg263, Gly271, and Leu290, providing a plausible explanation for the comparatively less favorable docking score in the absence of a directional polar anchor (Figure 3C). The shared recruitment of Arg263 and the Phe/Val/Met-rich pocket environment across all three complexes supports targeting of the BH3 groove as a mechanistic basis for anti-apoptotic inhibition, a strategy that remains central in current Mcl-1 inhibitor discovery and optimization [30].

Molecular dynamics simulation

Molecular docking provides a static, structure-based estimate of ligand accommodation within a protein binding cavity by proposing plausible binding orientations and corresponding scoring values. In contrast, molecular dynamics (MD) simulations model the time-dependent behavior of the protein-ligand system under an explicit force field, thereby capturing conformational flexibility, solvent-mediated effects, and thermal fluctuations that influence the integrity of the complex. Within structure-based drug discovery workflows, docking supplies commonly ranked starting poses, whereas MD enables evaluation of pose persistence, binding-site adaptation, and conformational rearrangements consistent with induced-fit phenomena that are not represented in rigid or semi-rigid docking treatments [31]. Accordingly, descriptors such as root mean square deviation (RMSD), root mean square fluctuation (RMSF), radius of gyration (Rg), solvent-accessible surface area (SASA), and number of hydrogen bonds (Hbonds) are routinely interpreted as complementary indicators of equilibration, local mobility, global compactness, and interaction continuity in protein-ligand systems. Consequently, the total energy and potential energy values for the CPD2-6QFQ complex were found to be -221,444 kJ/mol and -275,387 kJ/mol, respectively. For the Fruquintinib-6QFQ complex, the total energy and potential energy values were measured at -221,350 kJ/mol and -275,258 kJ/mol, respectively. The simulation system maintained equilibrium at a temperature of 300 K.

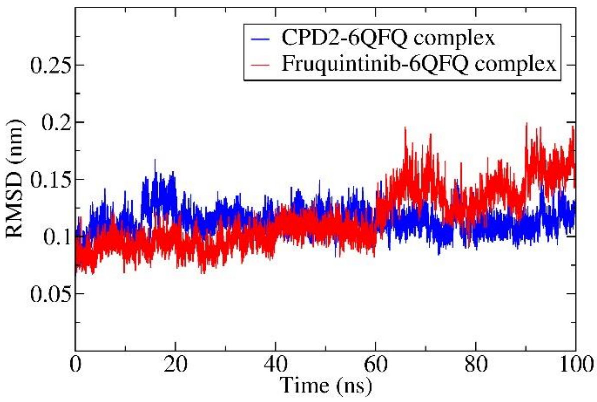

A

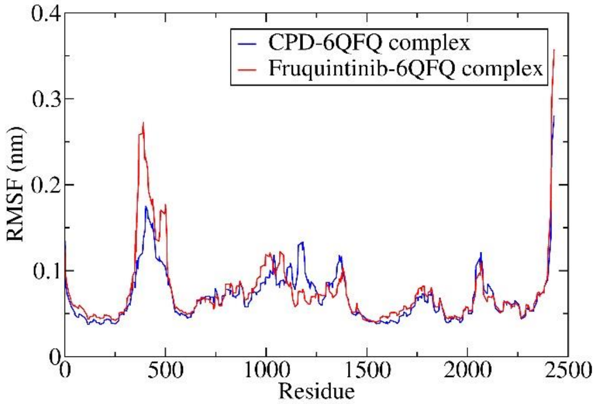

B

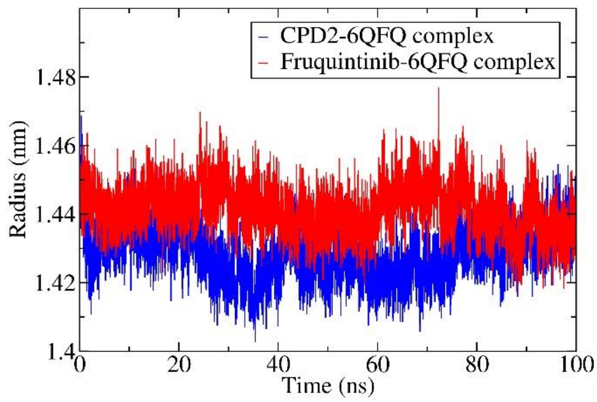

C

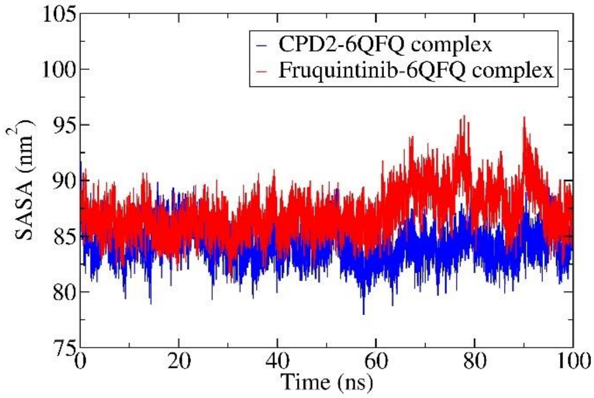

D

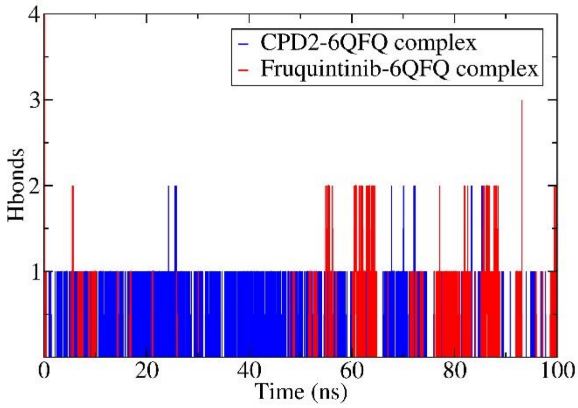

E

Figure (4): Results of MD simulation for the bindings of CPD2 (blue) and Fruquintinib (red) with 6QFQ protein. (A) RMSD, (B) RMSF, (C) Rg, (D) SASA, (E) Hbonds.

The RMSD indicates distinct late-trajectory behavior for the two complexes. The CPD2-6QFQ trajectory remains confined to a comparatively narrow band for most of the 100 ns window (typically near 0.10-0.13 nm, with transient excursions early in the simulation), consistent with limited backbone displacement after initial relaxation. In contrast, the Fruquintinib-6QFQ system follows a similar range during the early and mid stages but shows a clear upward shift after approximately 60 ns, with values frequently approaching 0.15-0.18 nm and reaching 0.20 nm near the end of the run (Figure 4A). Such sustained elevation is commonly interpreted as progressive conformational adjustment of the receptor-ligand ensemble rather than short-lived thermal noise [32].

When RMSF interpretation is restricted to the Asp172-Val321 segment, residue-wise fluctuations remain generally low for both complexes, with most positions exhibiting amplitudes predominantly below 0.10 nm, consistent with preservation of the local secondary-structure framework that delineates the Mcl-1 recognition corridor (Figure 4B). Within this window, elevated mobility is confined to a limited subset of positions, including the segment corresponding to the first prominent peak of the trace and the C-terminal end of the interval. Across the early peak, Fruquintinib-6QFQ shows higher fluctuation amplitudes than CPD2-6QFQ, paralleling the higher global RMSD behavior of the Fruquintinib-bound system and indicating increased local plasticity within the analyzed region. Importantly, residues that define the groove environment highlighted by docking, particularly His224, Ala227, Phe228, Met231, Val249-Val253, Phe254, Gly262, Arg263, Thr266, Leu267, Phe270, and Gly271, retain comparatively restrained RMSF values in both trajectories, supporting maintenance of a stable pocket architecture while allowing ligand-dependent micro-adjustments compatible with induced-fit accommodation.

The Rg further differentiates overall compactness. CPD2-6QFQ maintains a slightly lower and more uniform Rg trajectory (approximately 1.41-1.44 nm), consistent with a more compact conformational ensemble (Figure 4C). Fruquintinib-6QFQ remains shifted toward higher values (commonly 1.43-1.46 nm) and displays broader excursions, including brief increases toward 1.47-1.48 nm. In parallel, SASA (Figure 4D) is systematically higher for Fruquintinib-6QFQ (often occupying the upper portion of the 80-95 nm^2 axis range and increasing after 60 ns), whereas CPD2-6QFQ trends lower with reduced dispersion. Joint elevation of Rg and SASA is widely associated with increased solvent exposure and partial loosening of tertiary packing, which may accompany groove breathing motions during ligand residence.

The Hbonds time series indicates that hydrogen bonding is intermittent in both systems, but with different temporal patterns. CPD2-6QFQ shows predominantly 0-1 hydrogen bonds across most of the simulation, with occasional short-lived spikes to 2 (Figure 4E). Fruquintinib-6QFQ exhibits more frequent periods with 1-2 hydrogen bonds after roughly the mid-trajectory region, alongside sporadic excursions to higher counts. This pattern suggests that Fruquintinib can access additional transient polar contacts during later conformational adjustment; however, the concurrent rise in RMSD and solvent exposure indicates that increased hydrogen-bond sampling does not necessarily translate into tighter global stabilization. In the Mcl-1 BH3 groove, affinity and residence are often dominated by hydrophobic pocket complementarity. At the same time, polar anchoring, frequently involving hotspot residues such as Arg263, contributes to specificity and pose selection rather than guaranteeing reduced receptor mobility.

Collectively, the combined metrics support a more conformationally stable protein ensemble for CPD2-6QFQ, characterized by lower RMSD drift, slightly increased compactness (lower Rg), and reduced solvent exposure (lower SASA), despite the limited occurrence of long-lived hydrogen bonding. Fruquintinib-6QFQ exhibits greater late-stage conformational plasticity, characterized by higher RMSD, increased Rg/SASA, and more frequent transient hydrogen-bonding events. Within the broader context of Mcl-1 inhibitor development, where modulation of a large, predominantly hydrophobic BH3-binding surface and engagement of groove hotspots govern potency and selectivity, these observations are consistent with ligand-dependent differences in groove remodeling propensity that can be resolved only under explicit dynamical sampling [33].

Free binding energy (MM/GBSA) analysis

MM/GBSA provides an end-point estimate of protein-ligand association by combining molecular-mechanics interaction terms (van der Waals and Coulombic electrostatics) with an implicit-solvent treatment in which the polar solvation component is represented by a generalized Born (GB) model and the nonpolar contribution is commonly approximated as a solvent-accessible surface area (SASA) term. Under consistent force-field parameterization and trajectory sampling, MM/GBSA is most reliably applied for relative ranking because configurational entropy is frequently omitted, and the resulting estimates can vary with dielectric assumptions and other model settings [34]. As summarized in the provided MM/GBSA decomposition, both complexes exhibit negative mean total binding free energies (ΔTOTAL), indicating favorable association in the MM/GBSA sense. Fruquintinib-6QFQ shows a more favorable mean estimate (ΔTOTAL = −29.25 ± 2.91 kcal/mol) than CPD2-6QFQ (ΔTOTAL = −24.45 ± 2.74 kcal/mol), supporting stronger predicted binding for Fruquintinib within the same computational protocol. This difference arises primarily from a more favorable gas-phase interaction term (ΔGGAS) for Fruquintinib (−46.40 ± 6.12 kcal/mol) relative to CPD2 (−43.38 ± 5.51 kcal/mol), driven mainly by enhanced van der Waals stabilization (ΔVDWAALS) (−39.26 ± 3.24 vs −33.87 ± 2.94 kcal/mol). In contrast, the electrostatic interaction term (ΔEEL) favors CPD2 (−9.51 ± 4.70 kcal/mol) over Fruquintinib (−7.14 ± 5.54 kcal/mol), indicating that the Fruquintinib advantage is not electrostatically dominated but instead reflects stronger dispersion/packing complementarity (Table 2) [35].

Table (2): Free energy of binding obtained using MM/GBSA calculations

Energy Component	Average (kcal/mol)		Standard Deviation	
	CPD2-6QFQ	Fruquintinib-6QFQ	CPD2-6QFQ	Fruquintinib-6QFQ
ΔVDWAΔALS	-33.87	-39.26	2.94	3.24
ΔEEL	-9.51	-7.14	4.70	5.54
ΔEGB	23.41	22.13	4.19	4.42
ΔESURF	-4.48	-4.97	0.40	0.36
ΔGGAS	-43.38	-46.40	5.51	6.12
ΔGSOLV	18.93	17.16	4.10	4.30
ΔTOTAL	**-24.45**	**-29.25**	**2.74**	**2.91**

Solvation opposes binding for both ligands, with positive ΔGSOLV values, yet Fruquintinib incurs a more minor net solvation penalty (17.16 ± 4.30 kcal/mol) than CPD2 (18.93 ± 4.10 kcal/mol). This reduced penalty is consistent with a slightly smaller polar desolvation term (ΔEGB) for Fruquintinib (22.13 ± 4.42 vs 23.41 ± 4.19 kcal/mol) together with a marginally more favorable nonpolar surface term (ΔESURF) (−4.97 ± 0.36 vs −4.48 ± 0.40 kcal/mol). The standard deviations for ΔTOTAL (2.7-2.9 kcal/mol) and the major components indicate moderate energetic dispersion across the sampled configurations, a behavior frequently reported for endpoint approaches that remain sensitive to conformational heterogeneity and implicit-solvent parameterization.

ADMET prediction analysis

ADMET profiling of CPD2 and Fruquintinib was generated using the pkCSM framework to support early developability triage by providing rapid, model-based estimates across absorption, distribution, metabolism, excretion, and toxicity domains (Table 3). In silico ADMET screening is commonly integrated with complementary platforms and decision-support resources during lead prioritization [36].

Absorption: Both compounds exhibited low predicted aqueous solubility, with CPD2 at −4.169 log mol/L and Fruquintinib at −4.409 log mol/L, indicating a marginally more favorable solubility estimate for CPD2 under the model. Predicted epithelial permeability favored Fruquintinib (Caco-2: 1.146 log Papp) relative to CPD2 (0.818 log Papp), consistent with the higher predicted human intestinal absorption for Fruquintinib (88.714%) compared with CPD2 (71.089%). Predicted skin permeability was comparable (CPD2 −2.903 log Kp; Fruquintinib −2.762 log Kp), suggesting slightly higher modeled transdermal permeation for Fruquintinib due to the less harmful value. Neither compound was classified as a P-glycoprotein substrate; however, both were predicted as P-gp I inhibitors, while P-gp II inhibition was predicted only for Fruquintinib. Given the recognized role of P-gp modulation in altering exposure and interaction risk at barrier tissues, the inhibitor signals warrant consideration in interaction-focused assessment [37].

Distribution: Predicted volume of distribution differed modestly, with CPD2 showing VDss = 0.033 log L/kg versus −0.02 log L/kg for Fruquintinib, suggesting slightly greater modeled tissue distribution for CPD2. The predicted fraction unbound (Fu) was higher for CPD2 (0.344) than for Fruquintinib (0.135), implying a larger unbound circulating pool for CPD2 within the model assumptions. Brain distribution indices were uniformly low: logBB was −1.069 (CPD2) and −0.934 (Fruquintinib), while logPS was −2.887 (CPD2) and −3.095 (Fruquintinib). As logBB and logPS are widely used quantitative descriptors for BBB penetration and CNS permeability in predictive modeling, these values collectively indicate limited CNS exposure for both compounds, with CPD2 showing a higher modeled CNS permeability (less negative logPS) [38].

Table (3): Predicted ADMET properties of CPD2 and Fruquintinib.

ADMET properties	Unit	CPD2	Fruquintinib
Water Solubility	(Log mol/L)	-4.169	-4.409
Caco2 permeability	(Log Papp in 10-6 cm/s)	0.818	1.146
Intestinal absorption (Human)	(% Absorbed)	71.089	88.714
Skin permeability	(Log Kp)	-2.903	-2.762
P-glycoprotein substrate	Yes/No	No	No
P-glycoprotein I inhibitor	Yes/No	Yes	Yes
P-glycoprotein II inhibitor	Yes/No	No	Yes
VDss	(Log L/kg)	0.033	-0.02
Fraction unbound (human)	(Fu)	0.344	0.135
BBB permeability	(Log BB)	-1.069	-0.934
CNS permeability	(Log PS)	-2.887	-3.095
CYP2D6 substrate	Yes/No	No	No
CYP3A4 substrate	Yes/No	Yes	Yes
CYP1A2 inhibitor	Yes/No	No	Yes
CYP2C19 inhibitor	Yes/No	No	Yes
CYP2C9 inhibitor	Yes/No	No	No
CYP2D6 inhibitor	Yes/No	No	No
CYP3A4 inhibitor	Yes/No	No	Yes
Total clearance	(Log ml/min/kg)	1.395	0.832
Renal OCT2 substrate	Yes/No	No	No
AMES toxicity	Yes/No	No	No
Max. tolerated dose (human)	(Log mg/kg/day)	0.394	0.385
hERG I inhibitor	Yes/No	No	No
hERG II inhibitor	Yes/No	No	Yes
Oral rat acute toxicity (LD50)	(mol/kg)	3.021	2.974
Oral rat chronic toxicity (LOAEL)	(Log mg/kg_bw/day)	2.109	0.98
Hepatotoxicity	Yes/No	No	Yes
Skin sensation	Yes/No	No	No
Tetrahymena pyriformis toxicity	(Log ug/L)	0.284	0.296
Minnow toxicity	(Log mM)	3.467	1.245

Metabolism: Both molecules were predicted as CYP3A4 substrates and non-substrates of CYP2D6, indicating a shared dependence on CYP3A4-mediated biotransformation rather than CYP2D6 turnover. The inhibitory liability profile diverged: CPD2 was negative across the assessed CYP inhibition endpoints, whereas Fruquintinib was predicted to inhibit CYP1A2, CYP2C19, and CYP3A4, with CYP2C9 and CYP2D6 inhibition remaining negative. Because CYP inhibition is a primary mechanistic driver of pharmacokinetic drug-drug interactions, particularly when substrate and inhibitor roles converge on the same pathway, the combined CYP3A4 substrate + CYP3A4 inhibitor classification for Fruquintinib represents a higher interaction-alert signature in this panel than CPD2 [39].

Excretion: Predicted total clearance was higher for CPD2 (1.395 log mL/min/kg) than Fruquintinib (0.832 log mL/min/kg), consistent with faster modeled systemic elimination for CPD2 and comparatively greater persistence for Fruquintinib under the same prediction scheme. Both compounds were predicted to be non-substrates of renal OCT2, thereby reducing the likelihood that OCT2-mediated renal secretion is a dominant elimination mechanism in this context.

Toxicity: Both compounds were predicted to be AMES-negative and hERG I inhibitor-negative, consistent with an absence of flagged mutagenicity and a negative signal for the primary hERG inhibition endpoint in this model output. In contrast, hERG II inhibition was predicted for Fruquintinib but not for CPD2, indicating an electrophysiology-related alert specific to Fruquintinib in this dataset. As hERG-related cardiotoxicity remains a central safety concern that is frequently addressed with data-driven predictive modeling, this differential signal supports targeted follow-up for Fruquintinib [40]. The predicted maximum tolerated dose (human) was similar (0.394 vs 0.385 log mg/kg/day for CPD2 and Fruquintinib, respectively). Acute oral rat toxicity (LD50) was 3.021 mol/kg (CPD2) and 2.974 mol/kg (Fruquintinib). For chronic oral rat toxicity (LOAEL), CPD2 showed a value of 2.109 log mg/kg bw/day. In contrast, Fruquintinib showed a value of 0.98 log mg/kg bw/day, indicating that adverse effects were predicted at a lower dose for Fruquintinib in this endpoint. A hepatotoxicity alert was predicted for Fruquintinib but not for CPD2; given the continued emphasis on computational strategies to detect hepatotoxicity risk earlier in development, this distinction is notable for prioritization and subsequent validation planning. Skin sensitization was negative for both compounds. Aquatic toxicity proxies were similar for *T. pyriformis* (0.284 vs 0.296 log µg/L for CPD2 and Fruquintinib), while minnow toxicity differed substantially (3.467 vs 1.245 log mM), suggesting higher predicted aquatic toxicity potency for Fruquintinib, given the lower log mM value [41].

Overall interpretation: CPD2 exhibits a profile characterized by higher predicted solubility, lower Caco-2 permeability and intestinal absorption, a higher unbound fraction, and higher predicted clearance, alongside a generally cleaner CYP inhibition and toxicity flag pattern within the reported endpoints. Fruquintinib shows stronger modeled absorption (permeability and intestinal absorption), but presents a broader CYP inhibition signature (CYP1A2/CYP2C19/CYP3A4), a hERG II inhibition flag, and a hepatotoxicity alert, with lower predicted clearance and less favorable chronic toxicity (LOAEL) in this panel. These differences align with common ADMET decision frameworks that integrate transporter/CYP liabilities, CNS exposure indices (log BB/log PS), and toxicity prediction signals as early risk differentiators.

Quantum chemistry computation using the DFT method

DFT calculations were used to characterize the frontier molecular orbital (FMO) pattern and global conceptual-DFT reactivity descriptors of CPD2 relative to Fruquintinib (Table 4). EHOMO is commonly associated with electron-donation propensity, whereas ELUMO reflects electron-acceptance propensity; the HOMO-LUMO gap (ΔE) is frequently treated as an indicator of electronic responsiveness, where smaller gaps generally correspond to easier charge redistribution under external perturbation [42].

Table (4): Quantum descriptors of CPD2 and Fruquintinib.

Molecule	EHOMO (eV)	ELUMO (eV)	ΔE (eV)	μ (eV)	χ (eV)	η (eV)	σ (eV^{-1})	ω (eV)
CPD2	-6.6587	-4.1433	2.5154	-5.4010	5.4010	1.2577	0.7951	11.5969
Fruquintinib	-8.9955	0.6549	9.6504	-4.1703	4.1703	4.8252	0.2072	1.8021

EHOMO (eV): highest occupied molecular orbitals; **ELUMO (eV)**: lowest unoccupied molecular orbitals; **ΔE (eV)**: energy gap; **μ (eV)**: chemical potential; **χ (eV)**: electronegativity; **η (eV)**: hardness; **σ (eV^{-1})**: softness; **ω (eV)**: electrophilicity index.

CPD2 presented a higher-lying HOMO (EHOMO = −6.6587 eV) than Fruquintinib (−8.9955 eV), indicating a comparatively greater tendency for electron donation according to the orbital-energy interpretation. Fruquintinib, in contrast, displayed a deeper HOMO consistent with reduced donor propensity under the same descriptor scheme. In the acceptor channel, CPD2 exhibited a markedly lower LUMO (ELUMO = −4.1433 eV) than Fruquintinib (0.6549 eV), implying that CPD2 possesses a more energetically accessible acceptor orbital. The orbital separation showed a substantial divergence: CPD2 had a small ΔE = 2.5154 eV, whereas Fruquintinib showed a large ΔE = 9.6504 eV (Figure 5). This pattern is consistent with a more readily polarizable, electronically soft profile for CPD2 and a more electronically rigid profile for Fruquintinib. The chemical potential and electronegativity values further differentiated the electronic character. CPD2 displayed a more negative chemical potential (μ = −5.4010 eV) and higher electronegativity (χ = 5.4010 eV) than Fruquintinib (μ = −4.1703 eV; χ = 4.1703 eV), consistent with a stronger modeled driving tendency toward electron acquisition for CPD2. Hardness and softness followed the expected inverse relation: CPD2 showed lower hardness (η = 1.2577 eV) and higher softness (σ = 0.7951 eV^{-1}), whereas Fruquintinib exhibited higher hardness (η = 4.8252 eV) and lower softness (σ = 0.2072 eV^{-1}). Such trends align with standard conceptual-DFT interpretations in which softer systems undergo electronic deformation more readily during intermolecular interactions [43]. The electrophilicity index displayed the most pronounced separation: CPD2 showed ω = 11.5969 eV, while Fruquintinib presented ω = 1.8021 eV. Because ω is widely used as a global measure of electrophilic stabilization capacity in conceptual DFT, the substantially higher value for CPD2 indicates a stronger electrophilic signature relative to Fruquintinib within this descriptor set. This electronic profile may be compatible with interaction patterns that emphasize stabilization through charge-transfer and electrostatic contributions, whereas Fruquintinib is characterized by lower electrophilicity and higher hardness [44].

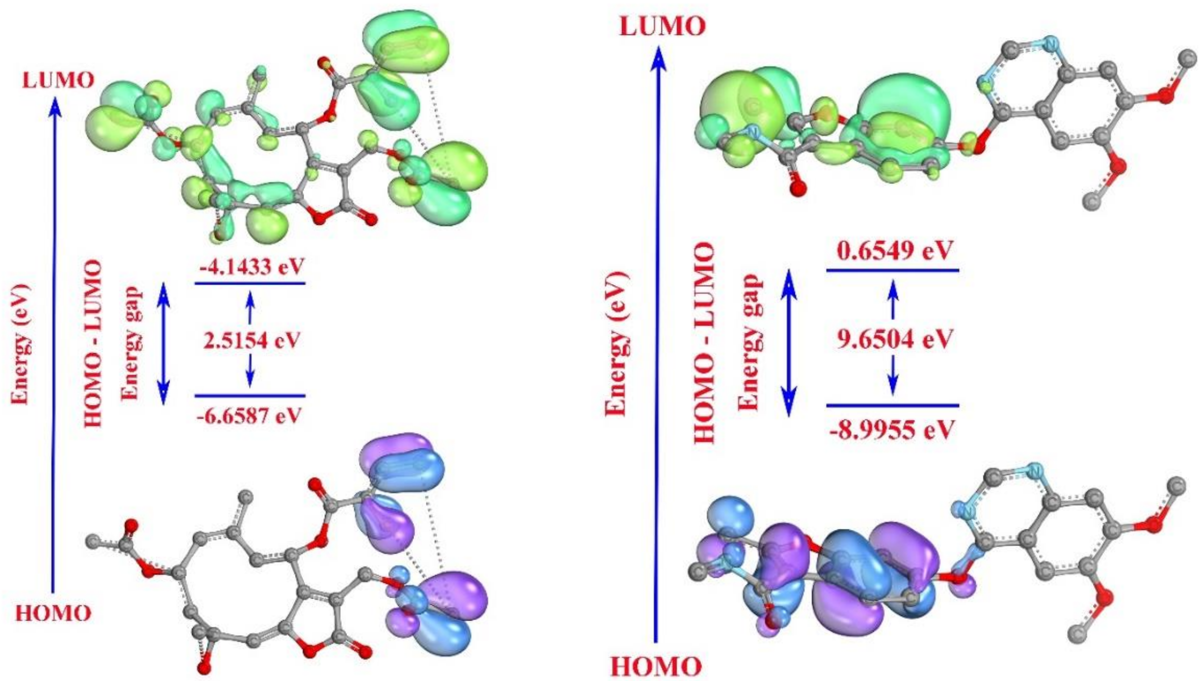

A B

Figure (5): HOMO and LUMO surface diagrams of CPD2 (A) and Fruquintinib (B).

Across FMO and global indices, CPD2 is characterized by higher HOMO energy, much lower LUMO energy, a narrow ΔE, greater softness, and markedly higher electrophilicity, collectively indicating greater electronic adaptability and electrophile-like behavior. Fruquintinib exhibits the opposite trend, characterized by a deep HOMO, high LUMO, wide ΔE, greater hardness, and lower electrophilicity, consistent with a more electronically stable and less readily polarizable scaffold under the same conceptual framework.

Conclusion

Computational modelling assessed CPD2 as an Mcl-1 (6QFQ)-directed candidate relative to Fruquintinib by integrating docking, molecular dynamics, MM/GBSA, ADMET prediction, and conceptual DFT descriptors. Docking placed the ligands within the BH3-binding groove and indicated a modest affinity advantage for CPD2 (−8.80 kcal/mol) over Fruquintinib (−8.33 kcal/mol), consistent with conserved engagement of the groove framework and a directed polar anchor at Arg263 for CPD2. Molecular dynamics suggested a more restrained CPD2-6QFQ ensemble across 100 ns, whereas the Fruquintinib-bound system exhibited greater late-trajectory deviation with increased solvent exposure despite intermittent hydrogen-bond sampling. MM/GBSA supported a favorable association for both ligands but favored Fruquintinib in mean end-point binding free energy (ΔTOTAL = −29.25 ± 2.91 kcal/mol) relative to CPD2 (−24.45 ± 2.74 kcal/mol), driven primarily by stronger van der Waals stabilization. In silico ADMET profiling differentiated developability-relevant liabilities: Fruquintinib combined higher predicted intestinal absorption with broader CYP inhibition and hepatotoxicity/hERG II alerts, whereas CPD2 showed fewer such flags alongside a higher predicted clearance (1.395 vs 0.832 log mL/min/kg). Conceptual DFT indices further separated intrinsic electronic behavior, with CPD2 exhibiting a narrow HOMO-LUMO gap (ΔE = 2.5154 eV) and higher electrophilicity (ω = 11.5969 eV) compared with Fruquintinib (ΔE = 9.6504 eV; ω = 1.8021 eV), suggesting greater electronic responsiveness for CPD2 under the applied descriptors. Overall, the integrated computational evidence supports CPD2 as a plausible optimization scaffold while clarifying ligand-dependent trade-offs between dynamical stability, end-point energetics, and safety-relevant prediction signals.

Nevertheless, computational prioritization remains conditional on experimental corroboration, and the present evidence is constrained by modelling assumptions and sampling limitations. The docking energies reflect scoring-function approximations, and pose-based interaction assignments do not guarantee persistence under physiological conditions. Although MD provided dynamic validation of complex behavior, a single 100 ns trajectory per ligand and reliance on one receptor conformation limit generalizability across alternative pocket states, and hydrogen-bond counts alone cannot resolve binding strength without kinetic or thermodynamic validation. MM/GBSA offers robust relative ranking under consistent protocols; however, the omission of configurational entropy and sensitivity to dielectric and solvation settings restricts quantitative interpretability. In silico ADMET outputs remain model-dependent and require confirmation using permeability, metabolic stability, transporter interaction, cardiotoxicity, and hepatotoxicity assays, particularly given the predicted CYP and safety flags for Fruquintinib. Quantum descriptors describe intrinsic electronic tendencies rather than direct biological reactivity, and off-target engagement, covalent liability, and polypharmacology were not assessed. Future work should prioritize biochemical binding measurements, cell-based efficacy evaluation in relevant cancer models, and pharmacokinetic-toxicity studies to establish translational relevance and to guide scaffold refinement toward improved potency, selectivity, and safety margins.

Disclosure Statements

- **Ethics approval and consent to participate:** Not applicable
- **Consent for publication:** Not applicable
- **Availability of data and materials:** The raw data required to reproduce these findings are available in the body and illustrations of this manuscript.
- **Author's contribution:** The sole responsibility for the conception of the study, presented results, and manuscript preparation. All data were generated in-house and that no paper mill was used.

- **Funding:** No funding was received to conduct this research.

- **Conflicts of interest:** The author declares that there is no conflict of interest regarding the publication of this article

- **Acknowledgements:** Not applicable.

Open Access

References

1] Bray F, Laversanne M, Sung H, Ferlay J, Siegel RL, Soerjomataram I, et al. Global cancer statistics 2022: GLOBOCAN estimates of incidence and mortality worldwide for 36 cancers in 185 countries. CA Cancer J Clin. 2024;74(3):229-63. https://doi.org/10.3322/caac.21834.

2] Johnson D, Chee CE, Wong W, Lam RCT, Tan IBH, Ma BBY. Current advances in targeted therapy for metastatic colorectal cancer - Clinical translation and future directions. Cancer Treat Rev. 2024;125. https://doi.org/10.1016/j.ctrv.2024.102700.

3] Haynes J, Manogaran P. Mechanisms and strategies to overcome drug resistance in colorectal cancer. Int J Mol Sci. 2025;26(5). https://doi.org/10.3390/ijms26051988.

4] Vogler M, Braun Y, Smith VM, Westhoff M-A, Pereira RS, Pieper NM, et al. The BCL2 family: from apoptosis mechanisms to new advances in targeted therapy. Signal Transduct Target Ther. 2025;10(1):91. https://doi.org/10.1038/s41392-025-02176-0.

5] Morris JL, Gillet G, Prudent J, Popgeorgiev N. Bcl-2 family of proteins in the control of mitochondrial calcium signalling: an old chap with new roles. Int J Mol Sci. 2021;22(7):3730. https://doi.org/10.3390/ijms22073730.

6] Mohiuddin M. Targeting MCL-1 to overcome therapeutic resistance and improve cancer mortality. Heal Sci Reports. 2025;8(10):e71390. https://doi.org/10.1002/hsr2.71390.

7] Yao W, Bai L, Wang S, Zhai Y, Sun S-Y. Mcl-1 levels critically impact the sensitivities of human colorectal cancer cells to APG-1252-M1, a novel Bcl-2/Bcl-XL dual inhibitor that induces Bax-dependent apoptosis. Neoplasia. 2022;29:100798. https://doi.org/10.1016/j.neo.2022.100798.

8] Zhu L, Wang W, Dong Y, Han X, Zhang W, Zhang Z, et al. Venetoclax synergizes with regorafenib for colorectal cancer by targeting BCL-2. Mol Carcinog. 2025;64(10):1683-96. https://doi.org/10.1002/mc.70017.

9] Tantawy SI, Timofeeva N, Sarkar A, Gandhi V. Targeting MCL-1 protein to treat cancer: opportunities and challenges. Front Oncol. 2023;13:2336289. https://doi.org/10.3389/fonc.2023.1226289

10] Fu D, Pfannenstiel L, Demelash A, Phoon YP, Mayell C, Cabrera C, et al. MCL1 nuclear translocation induces chemoresistance in colorectal carcinoma. Cell Death Dis. 2022;13(1):63. https://doi.org/10.1038/s41419-021-04334-y.

11] Nuzzo G, Senese G, Gallo C, Albiani F, Romano L, d'Ippolito G, et al. Antitumor potential of immunomodulatory natural products. Mar Drugs. 2022;20(6):386. https://doi.org/10.3390/md20060386.

12] Almansour NM, Allemailem KS, Abd El Aty AA, Ismail EI, Ibrahim MAA. In silico mining of natural products atlas (NPAtlas) database for identifying effective Bcl-2 inhibitors: molecular docking, molecular dynamics, and pharmacokinetics characteristics. Molecules. 2023;28(2):783. https://doi.org/10.3390/molecules28020783.

13] Uzun K, Bilen CY, Yalçın FN. Sesquiterpenes and prostate cancer. Phytochem Rev. 2025;24(5):3549-647. https://doi.org/10.1007/s11101-025-10088-8.

14] Abu-Izneid T, Rauf A, Shariati MA, Khalil AA, Imran M, Rebezov M, et al. Sesquiterpenes and their derivatives-natural anticancer compounds: An update. Pharmacol Res. 2020;161:105165. https://doi.org/10.1016/j.phrs.2020.105165.

15] Pan L, Lantvit DD, Riswan S, Kardono LBS, Chai H-B, Carcache de Blanco EJ, et al. Bioactivity-guided isolation of cytotoxic sesquiterpenes of *Rolandra fruticosa*. Phytochemistry. 2010;71(5):635-40. https://doi.org/10.1016/j.phytochem.2010.01.012.

16] Murray JB, Davidson J, Chen I, Davis B, Dokurno P, Graham CJ, et al. Establishing drug discovery and identification of hit series for the anti-apoptotic proteins, Bcl-2 and Mcl-1. ACS Omega. 2019;4(5):8892-906. https://doi.org/10.1021/acsomega.9b00611.

17] Van Der Spoel D, Lindahl E, Hess B, Groenhof G, Mark AE, Berendsen HJC. GROMACS: Fast, flexible, and free. J

Comput Chem. 2005;26(16):1701-18. https://doi.org/10.1002/jcc.20291.

18] Guex N, Peitsch MC. SWISS-MODEL and the Swiss-Pdb Viewer: An environment for comparative protein modeling. Electrophoresis. 1997;18(15):2714-23. https://doi.org/10.1002/elps.1150181505.

19] Zoete V, Cuendet MA, Grosdidier A, Michielin O. SwissParam: A fast force field generation tool for small organic molecules. J Comput Chem. 2011;32(11):2359-68. https://doi.org/10.1002/jcc.21816.

20] Pettersen EF, Goddard TD, Huang CC, Couch GS, Greenblatt DM, Meng EC, et al. UCSF Chimera-A visualization system for exploratory research and analysis. J Comput Chem. 2004;25(13):1605-12. https://doi.org/10.1002/jcc.20084.

21] Nguyen HD. Unveiling the anti-apoptotic mechanism of magnolialide as a colorectal cancer inhibitor via molecular modeling, ADMET, and MMGBSA analysis. Phys Chem Res. 2025;13(4):783-96. https://doi.org/10.22036/pcr.2025.535946.2708.

22] Jung W, Goo S, Hwang T, Lee H, Kim Y-K, Chae J, et al. Absorption distribution metabolism excretion and toxicity property prediction utilizing a pre-trained natural language processing model and its applications in early-stage drug development. Pharmaceuticals. 2024;17(3). https://doi.org/10.3390/ph17030382.

23] Neese F. Software Update: The ORCA program system-version 6.0. WIREs Comput Mol Sci. 2025;15(2):e70019. https://doi.org/10.1002/wcms.70019.

24] Knizia G, Klein JEMN. Electron flow in reaction mechanisms-revealed from first principles. Angew Chemie Int Ed. 2015;54(18):5518-22. https://doi.org/10.1002/anie.201410637.

25] Hanwell MD, Curtis DE, Lonie DC, Vandermeersch T, Zurek E, Hutchison GR. Avogadro: an advanced semantic chemical editor, visualization, and analysis platform. J Cheminform. 2012;4(1):17. https://doi.org/10.1186/1758-2946-4-17.

26] Sun E, Cohen FE. Computer-assisted drug discovery-a review. Gene. 1993;137(1):127-32. https://doi.org/10.1016/0378-1119(93)90260-A.

27] Ramírez D, Caballero J. Is it reliable to take the molecular docking top scoring position as the best solution without considering available structural data? Molecules. 2018;23(5)1038. https://doi.org/10.3390/molecules23051038.

28] Alhammadi SH, Baby B, Antony P, Jobe A, Humaid RS, Alhammadi FJ, et al. Modeling the binding of anticancer peptides and Mcl-1. Int J Mol Sci. 2024;25(12):6529. https://doi.org/10.3390/ijms25126529.

29] Ko D, Park S, Park M, Kim S, Park JM, Seo J, et al. Pitavastatin is a novel Mcl-1 inhibitor that overcomes paclitaxel resistance in triple-negative breast cancer. Exp Hematol Oncol. 2025;14(1):125. https://doi.org/10.1186/s40164-025-00716-6.

30] Liu J, Yin F, Wang Z, Song T, Zhang Z. An updated patent review of Mcl-1 inhibitors (2020-2022). Expert Opin Ther Pat. 2023;33(5):371-83. https://doi.org/10.1080/13543776.2023.2219394.

31] Santos LHS, Ferreira RS, Caffarena ER. Integrating molecular docking and molecular dynamics simulations. In: de Azevedo Jr. WF, editor. Docking screens for drug discovery. New York: Springer; 2019. p. 13-34. https://doi.org/10.1007/978-1-4939-9752-7_2.

32] Carugo O, Pongor S. A normalized root-mean-spuare distance for comparing protein three-dimensional structures. Protein Sci. 2001;10(7):1470-3. https://doi.org/10.1110/ps.690101.

33] Bolomsky A, Vogler M, Köse MC, Heckman CA, Ehx G, Ludwig H, et al. MCL-1 inhibitors, fast-lane development of a new class of anti-cancer agents. J Hematol Oncol. 2020;13(1):173. https://doi.org/10.1186/s13045-020-01007-9.

34] Adediwura VA, Koirala K, Do HN, Wang J, Miao Y. Understanding the impact of binding free energy and kinetics calculations in modern drug discovery. Expert Opin Drug Discov. 2024;19(6):671-82. https://doi.org/10.1080/17460441.2024.2349149.

35] Wang S, Sun X, Cui W, Yuan S. MM/PB(GB)SA benchmarks on soluble proteins and membrane proteins. Front Pharmacol. 2022;13:1018351. https://doi.org/10.3389/fphar.2022.1018351

36] Komura H, Watanabe R, Mizuguchi K. The trends and future prospective of in silico models from the viewpoint of ADME evaluation in drug discovery. Pharmaceutics. 2023;15(11):2619. https://doi.org/10.3390/pharmaceutics15112619.

37] Veiga-Matos J, Morales AI, Prieto M, Remião F, Silva R. Study models of drug-drug interactions involving p-glycoprotein: the potential benefit of p-glycoprotein modulation at the kidney and intestinal levels. Molecules. 2023;28(22):7532. https://doi.org/10.3390/molecules28227532.

38] Cornelissen FMG, Markert G, Deutsch G, Antonara M, Faaij N, Bartelink I, et al. Explaining blood-brain barrier permeability of small molecules by integrated analysis of different transport mechanisms. J Med Chem. 2023;66(11):7253-67. https://doi.org/10.1021/acs.jmedchem.2c01824.

39] Lee J, Beers JL, Geffert RM, Jackson KD. A review of cyp-mediated drug interactions: mechanisms and in vitro drug-drug interaction assessment. Biomolecules. 2024;14(1):99. https://doi.org/10.3390/biom14010099.

40] Falcón-Cano G, Morales-Helguera A, Lambert H, Cabrera-Pérez M-Á, Molina C. hERG toxicity prediction in early drug discovery using extreme gradient boosting and isometric stratified ensemble mapping. Sci Rep. 2025;15(1):15585. https://doi.org/10.1038/s41598-025-99766-3.

41] Khan MZI, Ren J-N, Cao C, Ye H-Y-X, Wang H, Guo Y-M, et al. Comprehensive hepatotoxicity prediction: ensemble model integrating machine learning and deep learning. Front Pharmacol. 2024;15:1441587. https://doi.org/10.3389/fphar.2024.1441587.

42] Magaji B, Singh P, Skelton AA, Martincigh BS. A density functional theory study of a series of symmetric dibenzylideneacetone analogues as potential chemical UV-filters. Heliyon. 2024;10(21):e39910. https://doi.org/10.1016/j.heliyon.2024.e39910.

43] Bhatia M. An overview of conceptual-DFT based insights into global chemical reactivity of volatile sulfur compounds (VSCs). Comput Toxicol. 2024;29:100295. https://doi.org/10.1016/j.comtox.2023.100295.

44] Pal R, Chattaraj PK. Electrophilicity index revisited. J Comput Chem. 2023;44(3):278-97. https://doi.org/10.1002/jcc.26886.